

TransPath: A Computational Method to Study the Ion Transit Pathways in Membrane Channels

Zhifeng Kuang,^a Anping Liu,^a and Thomas L. Beck^{a,b, 1}

Department of Chemistry^a

Department of Physics^b

University of Cincinnati

Cincinnati, OH 45221-0172

November 19, 2018

Abstract

The finely tuned structures of membrane channels allow selective passage of ions through the available aqueous pores. In order to understand channel function, it is crucial to locate the pore and study its physical and chemical properties. Recently obtained X-ray crystal structures of bacterial chloride channel homologues reveal a complicated topology with curvilinear pores. The commonly used HOLE program encounters difficulties in studying such pores. Here we propose a new pore-searching algorithm (TransPath) which uses the Configurational Bias Monte Carlo (CBMC) method to generate transmembrane trajectories driven by both geometric and electrostatic features. The trajectories are binned into groups determined by a vector distance criterion. From each group, a representative trajectory is selected based on the Rosenbluth weight, and the geometrically optimal path is obtained by simulated annealing. Candidate ion pathways can then be determined by analysis of the radius and potential profiles. The proposed method and its implementation are illustrated using the bacterial KcsA potassium channel as an example. The procedure is then applied to the more complex structures of the bacterial *E. coli* ClC channel homologues.

¹To whom correspondence should be addressed: becktl@email.uc.edu

1 Introduction

Ion channels comprise an important class of membrane proteins which control the selective passage of ions into and out of the cell (1). They possess aqueous pores through which the ions pass when the channel is in the open state. Many physiological functions in living cells are regulated by selectively translocating ions through a channel pore. The study of the physical and chemical properties of the pore provides clues concerning the function of an ion channel. These insights can aid in motivating site-directed mutagenesis studies and new drug design. With the advent of complex channel structures from X-ray crystallography, it is desirable to develop an effective computational tool to locate and display the pore, analyze the dimensions of the pore, identify the pore-lining residues, and produce the potential energy profile along the pore.

Several methods have been developed to display and analyze the surfaces of and cavities in proteins. These methods include the Connolly surface method (2), VOIDOO (3), PROACT (4), and SURFNET (5). A specially designed program, HOLE (6, 7), has been used for more than a decade to provide information about the variation of radius along a channel pore. This method is useful for relatively straight pores such as the gramicidin A and potassium channels. For complex structures like the ClC Cl⁻ channel homologues, however, it is difficult to use this method to locate and display the ion conduction pore due to the curvature feature, multiple pores, and possible blockage of the pore by residues in the protein.

The basic idea of the HOLE algorithm is to use a Monte Carlo simulated annealing procedure to find the largest radius of a probe sphere which can be accommodated along the length of the pore. HOLE moves the probe by taking only geometry into consideration. When there are multiple geometric pores, it is difficult for HOLE to distinguish an ion permeation pore from other energetically inaccessible pores during the hole searching process. In addition, HOLE requires a user to specify an initial point within the pore center and a direction of the pore alignment. That means that HOLE is specially designed for analyzing the dimensions of a known pore but not for searching for unknown pores. Finally, HOLE uses $\exp(R/K)$ as its importance sampling function, where R is the distance from the center of the probe to the edge of the nearest protein atom and K is a control constant analogous to the factor kT in equilibrium statistical mechanics. Due to the soft nature of the ‘energy’ $-R$, the procedure allows the probe to move through highly confined or even occupied regions of space. While the HOLE algorithm has limitations for complex topologies like the ClC Cl⁻ channel homologues, Monte Carlo (MC), molecular dynamics (MD), and Brownian dynamics (BD) simulation methods have been employed to study the ion permeation process (8, 9, 10, 11, 12). It is very time consuming, however, to calculate the full interaction energy for each step of ion motion.²

In order to address these issues, we propose a new method to generate transmembrane trajectories by taking advantage of the Rosenbluth self-avoiding random walk scheme (14,

²Other coarse-graining approaches have been developed to significantly extend the accessible timescales in studies of ion permeation (13).

15). The biased random walk approach allows for moves in the configuration space which may take place only over very long times in MD simulations. With the incorporation of continuous potential energy terms in the sampling function, the approach is termed the Configurational Bias Monte Carlo (CBMC) method, which has found wide application in polymer simulations (16, 17, 18). In our work, the sampling function includes contributions from both geometric and electrostatic features in the channels. These terms direct the biased random walk through open regions of space that are energetically favorable for ions with a specified charge.

Following the generation of an ensemble of membrane-traversing trajectories, we then utilize a simulated annealing technique similar to the HOLE method to find a unique and geometrically optimal path for analysis. The simulated annealing procedure is used to adjust each state to the center at which the largest sphere can be accommodated without overlapping any protein atoms. We utilize a harsher sampling function than is used in the HOLE method in order to prevent movement into highly restricted domains. Upon annealing, the trajectories typically collapse into one or a few protopaths. Finally we calculate the radius and potential profiles for each of these protopaths. By examination of both the radius and potential profiles, candidate ion conduction paths can be identified. This method has previously been employed in a detailed study of ion transit paths and gating in the bacterial ClC channel homologues (19, 20); here we present details of the algorithm. In our previous work, we focused on the extracellular side of the structures to explore chloride ion pathways, possible binding sites for chloride ions awaiting entry to the filter, multi-ion occupancy of the filter, proton access pathways approaching the fast gate, and the dependence of glutamate gate protonation on occupancy of the central region of the filter by chloride ions. In the present study we examine electrostatic effects on the intracellular side of the chloride channel homologues and relate our results to recent, related physiological experiments (21, 22).

In the Methods section, we describe the algorithm by taking the KcsA bacterial potassium channel as an example. The K^+ channel is a tetramer with four-fold symmetry about a central pore (23). From the intracellular side, the pore begins as a tunnel and then opens into a wide cavity. The other end of the cavity is connected to the narrow filter which separates the cavity from the extracellular solution. This well-defined pore has previously been analyzed with the HOLE method (23, 24, 25), so it serves as a benchmark for our algorithm. In the Results Section, we apply the method to the more complex *E. coli* ClC Cl^- channel homologues. The computational results are compared with experimental observations in the Discussion section.

2 Methods and Implementation

We numerically solve the variable-dielectric Poisson equation and thus generate the electrostatic potential due to the protein in the inhomogeneous dielectric environment. The problem is discretized on a cubic lattice. The lattice size is 0.5 Å. There are 257 mesh points in one direction, so the length of each side of the cube is 128 Å. The center of the cube is at the origin of a Cartesian coordinate system (x, y, z) . The 3D structure of the protein is

discretized with the CHARMM PBEQ subroutine (26) and mapped onto the center of the lattice. The z direction is perpendicular to the membrane, passing from the intracellular side (negative z) to the extracellular side (positive z) of the protein. The mass center of the protein coincides with the center of the cube. The Cardinal B-spline method is used for charge partitioning. The protein surface is created with a probe radius of 1.0 Å for the dielectric boundary. The protein is embedded in a dummy membrane modeled as a uniform dielectric medium without any charges or dipoles. The lattice is partitioned into three regions. The first region represents the protein and is characterized by a low dielectric constant $\epsilon_p = 4.0$. The second region includes the solvent reservoirs and all the cavities of the protein and is characterized by a high dielectric constant $\epsilon_w = 80.0$. The third region represents the membrane and is characterized by a low dielectric constant $\epsilon_m = 2.0$. We set the electrostatic potential to zero on the distant boundaries, and the potential is calculated with our fast multigrid Poisson solver (27). The salt concentration is set to zero for the work presented here.

As we have already mentioned, the first step of our method is to generate transmembrane trajectories of a probe ion through the channel by use of the CBMC scheme. For the simple case of hard-sphere lattice polymer simulations, a chain configuration is generated by first inserting a segment at a randomly selected site, and then inserting subsequent segments of the chain randomly at other available nearest-neighbour sites which are not occupied either by other molecules in the system or by any previously inserted segments. In the case that no free neighbour sites are available, the attempt to grow a trial chain configuration is abandoned. In this way, a continuous hole in a protein can be probed, so we suggest that the self-avoiding random walk (SAW) scheme of Rosenbluth and Rosenbluth (14) can be modified to search for the ion conduction pathway of a channel based on its X-ray crystal structure. The additional feature in the CBMC method is to employ a biased random walk where the Monte Carlo choice is based on the relative energetics for possible atom placements (in addition to excluded volume effects). Below we discuss the algorithm in detail.

Step 1. Find the first segment

We do not insert the first segment at a randomly selected site. Instead, we take advantage of the different dielectric constant assignments for the protein ($\epsilon_p = 4.0$) and cavity ($\epsilon_w = 80.0$) regions to locate all the high dielectric spots in a starting window bounded by $[xl, xr] \times [yl, yr] \times [zl, zr]$. The z window is typically narrow and is chosen near the center of the protein, and the x, y windows cover most of the protein in the plane parallel to the membrane. Since any ion pathway must pass through aqueous zones, an exhaustive search of all of the high-dielectric patches must contain the relevant pores. For each located high-dielectric spot, a simulated annealing process described below is performed to find the center at which the biggest sphere can be accommodated without overlapping with any protein atoms, and that high-dielectric spot is not revisited in searching for initial locations for trajectories. For the KcsA potassium channel, we chose $[-5, 5] \times [-5, 5] \times [-0.5, -0.5]$ as the starting window, a simple square near the center of the membrane. The first segment found is at $(0., 0., -0.5)$.

Step 2. Grow the chain

We generate a chain by use of a self-avoiding and biased random walk of a probe ion of charge q starting from one of the recorded first segments. The possible sites of a trial step are not neighbour lattice sites but as many randomly chosen sites on the surface of a sphere as desired. Hence, the motion is in continuous space. At the current step of the random walk, we bias the choice of the next step by comparing the Boltzmann weights (Eq. 1 below) of 20 random positions uniformly distributed on a $5/8$ sphere surface centered at the current position and pointed in the z direction. The sphere radius is chosen as 0.25 \AA . We select the next position j with a probability

$$P_j = \frac{e^{-E_j/K}}{\sum_{i=1}^n e^{-E_i/K}}, \quad (1)$$

where $n \leq 20$ is the total number of available sites excluding those positions which are occupied by protein atoms or previously generated segments. The energetic factor E_j is specified below, and K is a control constant analogous to a temperature. The product of the denominators in Eq. 1 for each added segment is termed the Rosenbluth weight for the fully grown chain.

Since ion motion across cell membranes has important contributions from the physical dimensions of the pore, the electrostatic potential due to the protein, and the membrane potential, we propose the following energetic cost term for the chain growth:

$$E_j = \omega_r/R + \omega_\phi q\phi + \omega_{bias} q\phi_{bias}, \quad (2)$$

where ϕ is the electrostatic potential due to the fixed protein charge distribution and ϕ_{bias} is an imposed extra potential which accounts for the membrane potential and nudges the biased random walk either up or down. ω_r , ω_ϕ , and ω_{bias} are scaling factors which can be adjusted. We have taken $\omega_r = 0.1$, $\omega_\phi = 1.0$, and $\omega_{bias} = 1.0$ to yield comparable magnitudes for all three terms. We have found that, in the generation of the transmembrane trajectories, it is better to maintain a relatively small value for ω_r ; the test ion motions are excluded from occupied regions but are otherwise largely driven along the biased random walk by electrostatic features. R is the distance from a trial position \mathbf{p} to the nearest van der Waals protein contact, which accounts for the physical dimension of the hole:

$$R = \min_{i=1}^N [|\mathbf{x}_i - \mathbf{p}| - r_i], \quad (3)$$

where \mathbf{x}_i is the position of a protein atom i or the previously occupied position of the probe ion, and r_i is the van der Waals radius of the atom or the probe ion. Our geometric contribution, ω_r/R , is proportional to the Born desolvation cost of moving an ion from an aqueous region into a spherical aqueous pore of radius R embedded in a large low-dielectric environment.

We note that, in a continuum dielectric model, the ion motion should include a self-energy term in addition to the electrostatic potential due to fixed protein charges. Thus,

the self-energy barrier due to the penalty of dehydration is missing in the energy function Eq. 2. If this term is included, the self energy must be calculated for each trial position, which would be computationally expensive. The self energy can be quite large in the narrow selectivity filter regions (19). One justification for neglecting the self-energy contribution is that, during the CBMC trajectories, we do already include a (relatively small) geometric term which directs the walk into open spaces, and this is related to a simple Born expression for desolvation in a spherical cavity (above). A second justification for the neglect of the self-energy term relates to small protein fluctuations about the ions in narrow regions of the pore. It has been shown that these fluctuations, while not appreciably altering the self-energy contribution, can lead to a large electrostatic stabilization energy which can nearly offset the self-energy penalty (28). All the calculations presented here are for rigid protein structures which don't include this stabilization effect countering the self energy. Thus, neglecting the self energy approximately accounts for this partial cancellation.

The above procedure is repeated step-by-step until either (a) the trajectory has walked out of the protein, or (b) it is blocked somewhere inside the protein. Those trajectories which do not make their way out of the protein are discarded. In turn, the whole process is restarted from the initially specified first segment by directing the 5/8 sphere surface in the opposite direction and reversing the external potential. The process of the CBMC random walk from the same starting point is repeated many times. Swarms of transmembrane trajectories are generated and recorded.

At this stage, ideally we should perform a simulated annealing process on all transmembrane trajectories to see if those starting from the same first segment will collapse into one or a few prototype paths. But we find this is expensive and not necessary. A more efficient way is to group the trajectories by comparing the vector distances between them as follows.

We choose a number of lattice layers perpendicular to z with equal distances of separation of 0.5 Å. The exact number and positions of the layers depend on the size of the protein and are automatically adjusted by the code. Each trajectory is represented by a vector where the elements are the intersection points between the trajectory and the layers.

We then take the vector of the first trajectory as the reference vector of the first group. Subsequently, we compute the distance between the reference vector and the second vector. If the distance is less than a given cutoff distance, we place it in the same group and take the average as a new reference vector; otherwise, a second group with its own reference vector is created. Screening all the vectors, we bin all trajectories into no more than 10 groups. From each group, we choose the trajectory with maximum Rosenbluth weight as the optimal trajectory. The averaged Rosenbluth weight is related to the excess chemical potential, and thus provides a sensible measure of favorable energetics for a given trajectory.

Step 3. Simulated annealing

Finally, a Metropolis Monte Carlo simulated annealing procedure is used to adjust each point \mathbf{p} along the selected trajectory to find the largest sphere whose center lies on the plane through \mathbf{p} and orthogonal to the z direction (6). Since the radius of a pore should be

larger than 0.5 Å, but the distance between two adjacent states of a trajectory is set to be 0.25 Å (the sphere radius for generating trial points), it is not necessary to implement the annealing procedure for each point on the trajectory. Rather, we perform the annealing on the corresponding vector obtained in the binning process described above.

Although we use a procedure similar to Smart *et al.* (6) for the annealing step, there are three features which differ. First, a potential profile along the center is also generated during the annealing process. This potential profile is the basis for identifying energetically favorable ion conduction pathways. Second, we use $1/R$ rather than $-R$ as the geometric ‘energy’ term; if R is negative, the energetic cost is taken as infinity which prevents the paths from ‘tunneling’ through occupied regions. Given a transembrane trajectory generated by the CBMC algorithm, this allows the annealing process to relax locally to the geometric center without moving large distances into neighboring geometrically accessible cavities. Third, the annealing procedure is performed in planes normal to \mathbf{z} , whereas in the HOLE algorithm the annealing is done in planes perpendicular to the chosen search direction. Otherwise, our algorithm is identical to that in Ref. (6), and the reader is referred there for details. The annealing step locates the geometric center for the trajectory produced in the CBMC procedure discussed above.

We choose the initial annealing control constant K to be very small (0.001). In this case, the random walk goes steadily downhill since only moves that increase the distance R are accepted. With a relatively small maximum step size (0.2 Å), this ensures that the annealing finds a minimum in the energy function (that is, a maximum empty sphere size) near the already generated trajectory. In addition, we choose to use the hard-core radius as opposed to the van der Waals radius employed during the CBMC process (6). The hard-core radii are typically smaller than the van der Waals radii, and use of the hard-core values during the CBMC step leads to an excessively ‘open’ structure which allows for penetration of the chains into the protein. Smart *et al.* (6) argue, however, that the hard-core radii may give a slightly better estimate of pore radii which includes some degree of pore fluctuations in an average sense. Therefore, once the transmembrane trajectories are generated, we employ the hard-core values for the final relaxation to the geometric center.

The generated \mathbf{p}_{new} , $R(\mathbf{p}_{new})$, the electrostatic potential $\phi(\mathbf{p}_{new})$, and the index of the closest protein atoms to \mathbf{p}_{new} are recorded following the annealing process. The potential $\phi(\mathbf{p}_{new})$ at \mathbf{p}_{new} is calculated by a weighted-average interpolation scheme. The potential at a location not on a grid point is taken as the average from the neighboring eight grid points weighted by the relative volume of each sector within the cube. We shall refer to the functions $(\mathbf{p}_{new}(z), R(\mathbf{p}_{new}))$ and $(\mathbf{p}_{new}(z), \phi(\mathbf{p}_{new}))$ as the radius profile and potential profile of the pore. The radius profile provides information concerning the geometry of the pore. The potential profile provides clues about the function of the pore. The closest protein atom index is a representation of the pore-lining residues. Based on both the potential profile and the radius profile, possible ion conduction pathways can be sorted.

Our TransPath searching on the KcsA channel utilized membrane and protein dielectric constants of 4 and a water value of 78 to compare with the results in Ref. (25). The structure was taken from the X-ray crystal determination in (23) (PDB code 1BL8). Hydrogens and

missing atoms were added with the CHARMM (26) utilities, and were not relaxed. The default charge state was assumed in order to compare with the lowest curve in Fig. 5 of Ref. (25). The resulting path moves along a straight line down the center of the channel, as observed in Ref. (23). Fig. 1 displays the radius and potential profiles along the KcsA channel. The radius profile obtained from TransPath is superimposable on the corresponding profile from HOLE for the same structure. The potential profile is very close to that in Ref. (25), except the potential well near the intracellular channel entrance is not as deep for our path. This is likely due to slightly different placement (compared with Ref. (25)) of missing charged R117 atoms near the mouth of the pore. We do not repeat variations of the charge states or the interpretations of the results since they appear in the cited literature. In the next section, we apply the procedure described above to the more complex bacterial ClC Cl⁻ channel homologues.

3 Application to the Bacterial ClC Channel Homologues

Eukaryotic ClC chloride channels control the selective flow of small anions across membranes. They are involved in such physiological functions as the acidification of intracellular vesicles, excitability of skeletal muscle, and salt and water transport across epithelia (29). They also are involved in several inherited diseases (30). The channel gating is voltage and pH sensitive (31), and the chloride ion itself participates in the fast gating process (32, 33). Chloride channels are less selective than cation (sodium and potassium) channels, allowing a range of anions to pass under electrochemical gradients, and they exhibit multi-ion conduction (33). Prokaryotic homologues of the chloride channels have been shown to function in the acid response of *E. coli* by creating electrical shunts to balance the charge when protons are pumped out of the organism during exposure in the stomach (34).

In addition, it has recently been discovered that the bacterial homologues are not channels but proton/chloride antiporters (35). In our previous work on the bacterial structures (19), we investigated proton access pathways to the gate from the extracellular side. We also observed an apparent electrostatic conduit for protons from the gate to the intracellular side of the channel homologues. Three acid residues on the intracellular side of the bacterial channel homologue are replaced by basic or nonpolar residues in the ClC-0 channel, and a homology model (unpublished) displays no negative-potential conduit for protons to move all the way through the channel. Mutations of the acidic groups along the proposed proton pathway would provide interesting evidence as to how protons migrate across the bacterial structures. Previous mutagenesis studies, however, have indicated a close structural similarity between the prokaryotic and eukaryotic structures, so the functional difference may result from quite subtle changes in the proteins through evolution (29, 35).

Recently, X-ray crystal structures have been determined for the bacterial chloride channel homologue and two mutants (36, 37). These structures have confirmed the double-barrelled nature of the channels previously indicated by physiological experiments (38). The

dimeric structures exhibit a highly complex topology, each monomer containing 18 α -helices with a range of orientations relative to the membrane plane. Conserved sequences define the selectivity filter; they occur at the N-termini of several helices, creating a strong positive potential at a central anion binding site. Computational studies have shown that the binding energy is largely due to local interactions and not overall helix dipole effects (39).

The pore of the bacterial structures displays a curved hourglass structure, with a narrow selectivity filter separating two vestibules. In the wild-type structure, a glutamate residue (E148) occludes the pore on the extracellular side of the filter, while in the two mutant structures (E148A and E148Q) the side chain has moved out of the pore. This suggests a gating function for this strategically placed residue. Site-directed mutagenesis studies support this picture (37), but experiments utilizing intracellular anionic blocking agents have suggested that more extensive conformational changes may be involved in gating (40). The crystal structures display three anion binding sites: one at the intracellular entrance to the filter (S_{int}), one in the middle of the filter (S_{cen}), and one near the extracellular end of the filter (S_{ext}). The last site is occupied either by the glutamate gate or a chloride ion. In addition, an extracellular binding site (S_{bs}) has been proposed for chloride ions prior to entering the filter (9, 12, 19, 32, 39); this site is near the positively charged residues R147 and R340 and is adjacent to the E148 gate.

Several computational studies have appeared recently concerning the modeling of the chloride channels and their bacterial homologues. These efforts have focused on the ion transit pathways (12, 19), multi-ion occupancy of the pore (10, 11, 19, 39), the conduction mechanism (10, 11), the current-voltage behavior (11), pH dependent gating induced by chloride ion occupancy at the S_{cen} and S_{bs} sites (8, 9, 19, 20), and interactions of blocking agents with the intracellular side of the pore (41). A wide range of computational techniques has been employed, including electrostatics calculations and molecular dynamics, Monte Carlo, and Brownian dynamics simulations. Here we apply the TransPath technique described above to examine ion transit pathways on the intracellular side of the bacterial chloride channel homologues. We also examine electrostatic changes at the S_{int} site due to mutations designed to mimic recent site-directed mutagenesis studies of the ClC-0 channel (21, 22).

We first consider the wild-type *E. coli* structure (PDB code 1OTS) in which the E148 residue blocks the extracellular end of the selectivity filter. This provides a good test of the TransPath algorithm since the HOLE method encounters difficulties near the constricted gate region. HOLE searches tend to wander off into the protein near the obstructing E148 side chain.

For the TransPath pore searching, the starting region was confined to the domain $[-6, 6] \times [-27, -14] \times [-10, 8]$ (subunit A). The z domain was chosen over a larger range since two chloride ions and E148 were resolved in this region in the X-ray structure in subunit A. In addition, there is a binding site S_{bs} adjacent to R147 (and R340) near the extracellular entrance to the filter (19, 39). The parameters used in the searching processes were $\omega_r = 0.1$; $\omega_\phi = 1.0$; $\omega_{bias} = 1.0$; $\phi_{bias} = 150mV$; $K = 1.0$ for the CBMC searches, $K = 0.1$ for the initial control constant while searching for high dielectric spots, $K = 0.001$ for the initial control constant for the geometric annealing step, and $D_{max} = 0.2 \text{ \AA}$ (maximum step size

during simulated annealing). The default charge state was assumed (see below).

From the starting domain, sets of successful transmembrane trajectories were generated from 12 different high dielectric spots. In each of the 12 sets, 10 groups were generated, and from each group one trajectory was chosen based on the Rosenbluth weight. Each of these 120 trajectories was then annealed, and only several unique paths were located. By examining the radius and potential profiles, two prototypes were found favorable for chloride permeation on the intracellular side as shown in Fig. 2a. The radius and potential profiles are shown in Fig. 3.

The two anion transit pathways are identical for z values greater than -10 \AA . This region corresponds to the selectivity filter (roughly $-10 < z < 5 \text{ \AA}$) and the extracellular vestibule ($z > 5 \text{ \AA}$). The binding site S_{int} is located at $z = -8.7 \text{ \AA}$, which is at the origin of the filter on the intracellular side of the protein. The narrow constriction near the E148 residue of the wild-type structure is apparent in the radius profile ($0 < z < 5 \text{ \AA}$; $z = 1.0 \text{ \AA}$ for the S_{ext} site) (Fig. 3a). A larger radius is also observed near $z = -2.7 \text{ \AA}$ where an ion is located in the crystal structure at S_{cen} . It is clear from the radius profile near $z = -6 \text{ \AA}$ that protein fluctuations are required to allow ion transit from the intracellular side towards the S_{cen} site, since the radius is less than the ionic radius of a chloride ion; the side chain of S107 is located at $z = -5.5 \text{ \AA}$ and contributes to the decreased radius there. Both paths pass through the two anion binding sites S_{int} and S_{cen} and near the E148 obstruction at S_{ext} . The potential profile (Fig. 3b), while positive through the whole filter, is significantly reduced in magnitude relative to the two mutant (open) structures near the E148 side chain (19); it is large enough to bind an ion at the S_{cen} site (19, 39), but the pore is closed to chloride permeation due to the small radius and less favorable potential near S_{ext} . Finally, an extracellular vestibular anion binding site (S_{bs}) is apparent as a shoulder in the potential in the range $7 < z < 11 \text{ \AA}$. Two basic residues (R147 and R340) are located in close proximity to this site.

The two paths differ in the intracellular vestibule. One path (P1) displays a large radius and positive potential for $z < -10 \text{ \AA}$, while the other (P2) exhibits a reduction of radius and rapid potential variation. The path P1 moves through the more open vestibule region, while the path P2 passes near the α -helices D and R. The potential peak near $z = -19 \text{ \AA}$ is predominantly due to the R120 residue between helices D and E, while the valley near $z = -16 \text{ \AA}$ mainly results from the E111 residue in helix D (36). These results suggest that the dominant path for chloride entrance to the filter is P1 since the P2 path has an unfavorable potential energy near $z = -16 \text{ \AA}$. Finally, the pore-lining residues of the paths in Fig. 2a include the key residues Glu148, Phe357, Tyr445 and Ser107 which define the filter (36).

For the wild-type (1OTS) structure, the potential at S_{int} is 0.230 V (this value differs slightly from our earlier work (19) since chain A was used in the present study as opposed to chain B previously). When a chloride ion is added to the S_{cen} binding site, the potential drops to 0.114 V. It has been shown that the residue E113 is likely protonated due to a potential shift caused by the nearby E203 side chain (39). When we protonate E113, the potential at S_{int} with a chloride at S_{cen} becomes 0.178 V (potential shift of roughly $2kT$ relative to

the unprotonated form). This shift has been found to be necessary to ensure favorable free energies of binding of a chloride ion at the S_{int} site with ions occupying the S_{cen} and S_{ext} sites (39). In our previous work, we found a strong electrostatic well for chloride ions at the S_{ext} site (mutant structure 1OTU), even when the S_{cen} site was occupied by another anion. These computational results support the picture of multi-ion occupancy of the pore observed experimentally (33, 36, 37).

Recent single-channel measurements have shown a strong effect of the residues E127 and K519 on ClC-0 channel permeation and gating (21, 22). The two residues are believed to be located in helices corresponding to the helices D and R from the bacterial channel homologues, respectively, based on sequence alignment (36). The locations are near the intracellular entrance to the filter. The experimental results indicate an electrostatic influence, but it was found not to be due to a simple surface charge effect. This is likely due to the fact that the S_{int} binding site is at the entrance to the filter so that charge screening by large non-permeating ions is not easily achieved. A two-site kinetic model of the data was proposed: equilibrium binding to the S_{int} site followed by passage of the ion to a central binding site (S_{int}) and escape to the extracellular solution. In this model, the rate-limiting step for saturated concentrations was proposed to be the final escape to the solution. Mutations of the E127 and K519 residues in ClC-0 can affect the binding affinity and the rate of passage into the filter (first two steps of the model). Here we focus on electrostatic changes that might influence the affinity for binding at S_{int} and the rate constant for passage into the filter binding site S_{cen} .

E127 from ClC-0 corresponds to E111 in the *E. coli* channel homologue. K519 in ClC-0 aligns with T452 in the bacterial structure, however, and I518 aligns with R451. Therefore, we mutated R451 into I451 and T452 into K452 to mimic the expected local structure in ClC-0. Following the mutation, the side chains of the two residues were relaxed. Both the resulting E111 and K452 side chains are in close proximity to the anion pathway and the binding site S_{int} (Table 1).

For this work we utilized the mutant E148Q structure (PDB code 1OTU), in which the glutamine side chain is moved away from the S_{ext} binding site. We assumed the default charge state of E113 for these calculations since we are mainly interested in potential shifts due to the mutations at the S_{int} site. Anion pathways similar to those observed for the two mutants in our previous work were found (19). A swarm of representative trajectories is shown in Fig. 2b, which clearly displays the two vestibular regions separated by the narrow selectivity filter.

The mutation of the bacterial structure described above moves a positive charge more than 3 Å closer to the S_{int} binding site, and thus causes a positive shift in the potential relative to the original bacterial structure (Tables 1, 2). The potential shifts from 0.235 V for the 1OTU structure to 0.435 V for the I451/K452 mutant structure. This stronger binding energy at S_{int} (roughly 7 kT shift) may be one cause for increased conductance in the eukaryotic ClC-0 channel relative to the bacterial case (35).

Next, we performed eight mutations on the E111/K452 pair, sampling all possible charge states at these two sites. Neutral states were obtained by protonation of the glutamate

or deprotonation of the lysine. The results for the potential and the shift relative to the E111/K452 pair are shown in Table 2. First, notice that all potentials at S_{int} are positive, even in the presence of the E-E- mutation. Experimentally, the mutations corresponding to our mutations E-K+ (default ClC-0), E-K0, E-E-, E0K+, E0K0, E0E-, K+K+, and K+E- were made, and single-channel currents were measured (21). The wild-type E-K+ case exhibits the largest low concentration conductance, while the E-K0 and E-E- mutants show decreased conductances. All three mutants exhibited similar maximal conductances with increasing intracellular chloride ion concentration. This is consistent with an electrostatic effect on equilibrium binding at the S_{int} site due to the ClC-0 residue 519 charge state, where the decreasing potential (shifts of -0.245 V and -0.350 V) at S_{int} reduces anion occupancy.

The E0K+ and E0K0 ClC-0 mutants display conductance *vs.* chloride concentration curves very similar to the wild-type channel; the E0E- mutant displays slightly reduced conductance at low concentrations, but the conductance is significantly larger than for the E-E- mutant (21). These experimental findings suggest an important electrostatic role for E127 in the ClC-0 channel; the electrostatic effect of K519 is to some extent mediated by the negative charge on E127. The potential shifts for the mutations (E0K+, E0K0, and E0E-) are modest in magnitude, the largest value occurring for the E0E- mutant (-0.224 V or roughly $8 kT$). The experimental conductance *vs.* chloride ion concentration curve for the E0E- mutant lies between the wild-type curve and the E-K0 mutant; our potential shift calculation does not explain this difference in the maximal conductance since the potential shifts for E0E- and E-K0 are quite close. We note that our calculations are based on a fixed structure obtained from a simple homology model, and thus do not include any effect of protein fluctuations or significant relaxation from the bacterial X-ray structure.

The K+K+ mutant did not conduct (21); the electrostatic calculations yield a potential shift at S_{int} of 0.629 V (or roughly $23kT$). This very large positive shift likely binds the anions too strongly, thus reducing the driving force for ions to enter the filter and subsequently push ions at the S_{cen} site outwards towards the extracellular vestibule. The K+E- mutant did conduct, but with a maximal conductance roughly one half that of the wild-type channel. This result shows that charges at the E127 and K519 sites in ClC-0 do not influence conductance symmetrically. With the side chain placements in our calculations, we obtained a potential shift for this mutant of -0.053 V, a very small change, so our results do not rationalize the reduced maximal conductance observed experimentally. The kinetics of ion passage into the filter may be quite complicated and reflect important contributions from fluctuations; it was earlier proposed that the K519 residue may attract chloride ions towards the filter, while the E127 charge provides a push to drive the ions deep into the filter (21). All of these effects may be mediated by kinetic fluctuations in the local structure around the S_{int} binding site.

Therefore, our results shed some light on the electrostatic interpretation in Ref. (21); mutations of the E127 and K519 sites in ClC-0 that induce variations of the potential at S_{int} with magnitudes less than several kT do not dramatically change the channel conductances. However, if the potential change is too large in either the positive or the negative direction, currents can be significantly reduced or eliminated. We are not able to rationalize different

conductance curves for the E-K0 and E0E- mutants which exhibit similar potential shifts at S_{int} , nor changed maximal conductance for the K+E- mutant compared with wild-type ClC-0. This may be due to the simple homology model employed here, to protein fluctuations, or to limitations in a purely electrostatic interpretation. The results are consistent with the general picture that the residues E127 and K519 can provide electrostatic control of the affinity of chloride ions for the S_{int} site and perhaps the kinetics of ion access to the filter. Electrostatic control of access to the filter (S_{cen} and S_{ext} sites) via a “foot-in-the-door” mechanism has been implicated in the reduction of the channel closing rate with increasing intracellular chloride ion concentration (22) .

4 Conclusions

We have presented a new Monte Carlo algorithm for locating ion transit pathways through membrane proteins. The method is robust; it requires a protein structure, but does not rely on any prior knowledge of the pores which pass through the protein. The method first locates high dielectric spots in the center of the protein and then generates swarms of configurationally biased Monte Carlo trajectories which pass from one side of the membrane to the other. The trajectories are driven by both geometric and electrostatic features of the protein. Once energetically favorable membrane-spanning trajectories are produced, a subsequent annealing step based only on geometry locates a unique path through the protein. Analysis of the radius and potential profiles, along with a listing of pore-lining residues, yields useful information concerning the functioning of the channel. The method can be applied to study multiple ion transit pathways for ions of any charge.

The method was successfully tested on the potassium channel. Then, we examined possible chloride ion pathways on the intracellular side of the bacterial chloride channel homologues. The chloride channel is challenging due to multiple ion transit pathways, the curvature feature of the pores, and possible blockage of the pores by protein residues. The results were compared with recent physiological experiments on the ClC-0 channel which indicated important electrostatic effects near the intracellular entrance of the selectivity filter. The TransPath results shed light on the energetics resulting from a range of mutations on key charged residues. We are currently also utilizing the TransPath method in conjunction with molecular dynamics simulations to explore pore shape and energetic fluctuations induced by multi-ion passage through the filter of the ClC channel homologues.

5 Acknowledgements

We gratefully acknowledge the support of the Department of Defense MURI program. We thank John Cuppoletti, Danuta Malinowska, and Rob Coalson for many helpful discussions. Z. F. Kuang is grateful to Bob Eisenberg for bringing him to the ion channel field. The protein structures were displayed by VMD (42).

References

1. Hille, B. 2001. *Ionic Channels of Excitable Membranes*. Sinauer Associates, Sunderland, MA., 3rd edition.
2. Connolly, M. L. 1983. Solvent-accessible surfaces of proteins and nucleic acids. *Science*. 221:709–713.
3. Kleywegt, G., and T. A. Jones. 1994. Detection, delineation, measurement and display of cavities in macromolecular structures. *Acta Cryst.* D50:178–185.
4. Williams, M. A., J. M. Goodfellow, and J. M. Thornton. 1994. Buried waters and internal cavities in monomeric protein. *Protein Science*. 3:1224–1235.
5. Laskowski, R. A. 1995. SURFNET: a program for visualizing molecular surfaces. *J. Mol. Graphics*. 13:323–330.
6. Smart, O. S., J. M. Goodfellow, and B. A. Wallace. 1993. The pore dimensions of Gramicidin A. *Biophys. J.* 65:2455–2460.
7. Smart, O. S., J. G. Neduvilil, X. Wang, B. A. Wallace, and M. S. P. Sansom. 1996. HOLE: A program for the analysis of the pore dimensions of ion channel structural models. *J. Mol. Graphics*. 14:354–360.
8. Bisset, D., B. Corry, and S.-H. Chung. 2005. The fast gating mechanism in ClC-0 channels. *Biophys. J.* 89:179–186.
9. Bostick, D. L., and M. L. Berkowitz. 2004. Exterior site occupancy infers chloride-induced proton gating in a prokaryotic homolog of the ClC chloride channel. *Biophys. J.* 87:1686–1696.
10. Cohen, J., and K. Schulten. 2004. Mechanism of anionic conduction across ClC. *Biophys. J.* 86:836–845.
11. Corry, B., M. O’Mara, and S. H. Chung. 2004. Conduction mechanisms of chloride ions in ClC-type channels. *Biophys. J.* 86:846–860.
12. Miloshevsky, G. V., and P. C. Jordan. 2004. Anion pathway and potential energy profiles along curvilinear bacterial ClC Cl⁻ pores: Electrostatic effects of charged residues. *Biophys. J.* 86:825–835.
13. Siva, K., and R. Elber. 2003. Ion permeation through the gramicidin channel: atomically detailed modeling by the stochastic difference equation. *Proteins: Struct., Function, and Genet.* 50:63–80.
14. Rosenbluth, M. N., and A. W. Rosenbluth. 1955. Monte carlo calculation of the average extension of molecular chains. *J. Chem. Phys.* 23:356–359.

15. Siepmann, J. I., and D. Frenkel. 1992. Configurational bias monte carlo: a new sampling scheme for flexible chains. *Molecular Physics*. 75:59–70.
16. Beck, T. L., M. E. Paulaitis, and L. R. Pratt. 2005. *The Potential Distribution Theorem and Models of Molecular Solutions*. Cambridge, Cambridge.
17. Frenkel, D., and B. Smit. 2002. *Understanding Molecular Simulation: from Algorithms to Applications*. Academic Press, San Diego.
18. Siepmann, J. I. 1999. Monte carlo methods for simulating phase equilibria of complex fluids. *Adv. Chem. Phys.* 105:443–460.
19. Yin, J., Z. Kuang, U. Mahankali, and T. L. Beck. 2004. Ion transit pathways and gating in ClC chloride channels. *Proteins: Struct., Function, and Bioinform.* 57:414–421.
20. Yin, J., Z. Kuang, U. Mahankali, and T. L. Beck. 2005. Comment on ion transit pathways and gating in ClC chloride channels. *Proteins: Struct., Function, and Bioinform.* in press.
21. Chen, M.-F., and T.-Y. Chen. 2003. Side-chain charge effects and conductance determinants in the pore of ClC-0 chloride channels. *J. Gen. Physiol.* 122:133–145.
22. Chen, T.-Y., M.-F. Chen, and C.-W. Lin. 2003. Electrostatic control and chloride regulation of the fast gating of ClC-0 chloride channels. *J. Gen. Physiol.* 122:641–651.
23. Doyle, D. A., J. M. Cabral, R. A. Pfuetzner, A. Kuo, J. M. Gulbis, S. L. Cohen, B. T. Chait, and R. Mackinnon. 1998. The structure of the potassium channel: molecular basis of K⁺ conduction and selectivity. *Science*. 280:69–77.
24. Biggin, P. C., and S. P. Sansom. 2002. Open-state models of a potassium channel. *Biophys. J.* 83:1867–1876.
25. Ranatunga, K. M., I. H. Shrivastava, G. R. Smith, and S. P. Sansom. 2001. Side-chain ionization states in a potassium channel. *Biophys. J.* 80:1210–1219.
26. Brooks, B. R., R. E. Bruccoleri, B. D. Olafson, D. J. States, S. Swaminathan, and M. Karplus. 1983. CHARMM: a program for macromolecular energy, minimization, and dynamics calculations. *J. Comp. Chem.* 4:187–217.
27. Beck, T. L. 2000. Real-space mesh techniques in density functional theory. *Rev. Mod. Phys.* 72:1041–1080.
28. Mamonov, A. B., R. D. Coalson, A. Nitzan, and M. G. Kurnikova. 2003. The role of the dielectric barrier in narrow biological channels: a novel composite approach to modeling single-channel currents. *Biophys. J.* 84:3646–3661.
29. Estevez, R., and T. J. Jentsch. 2002. ClC chloride channels: correlating structure with function. *Curr. Opin. Struct. Biol.* 12:531–539.

30. Ashcroft, F. M. 2000. *Ion Channels and Disease*. Academic Press, New York.
31. Chen, M.-F., and T.-Y. Chen. 2001. Different fast-gate regulation by external Cl^- and H^+ of the muscle-type ClC chloride channels. *J. Gen. Physiol.* 118:23–32.
32. Chen, T.-Y., and C. Miller. 1996. Nonequilibrium gating and voltage dependence of the ClC-0 channel. *J. Gen. Physiol.* 108:237–250.
33. Pusch, M., U. Ludewig, A. Rehfeldt, and T. J. Jentsch. 1995. Gating of the voltage-dependent chloride channel ClC-0 by the permeant anion. *Nature.* 373:527–530.
34. Iyer, R., T. M. Iverson, A. Accardi, and C. Miller. 2002. A biological role for prokaryotic ClC chloride channels. *Nature.* 419:715–718.
35. Accardi, A., and C. Miller. 2004. Secondary active transport mediated by a prokaryotic homologue of ClC Cl^- channels. *Nature.* 427:803–807.
36. Dutzler, R., E. B. Campbell, M. Cadene, C. B. T., and R. Mackinnon. 2002. X-ray structure of a ClC chloride channel at 3.0 Å reveals the molecular basis of anion selectivity. *Nature.* 415:287–294.
37. Dutzler, R., E. B. Campbell, and R. Mackinnon. 2003. Gating the selectivity filter in ClC chloride channels. *Science.* 300:108–112.
38. Miller, C., and M. M. White. 1984. Dimeric structure of single chloride channels from torpedo electroplax. *Proc. Natl. Acad. Sci. USA.* 81:2772–2775.
39. Faraldo-Gomez, J. D., and B. Roux. 2004. Electrostatics of ion stabilization in a clc chloride channel homologue from *escherichia coli*. *J. Mol. Biol.* 338:981–1000.
40. Accardi, A., and M. Pusch. 2003. Conformational changes in the pore of CLC-0. *J. Gen. Physiol.* 122:277–293.
41. Moran, O., S. Traverso, E. L., and M. Pusch. 2003. Molecular modeling of p-chlorophenoxyacetic acid binding to the ClC-0 channel. *Biochem.* 42:5176–5185.
42. Humphrey, W., A. Dalke, and K. Schulten. 1996. VMD—visual molecular dynamics. *J. Mol. Graphics.* 14:33–38.

z locations of charged sites for 1OTS								
Residues	S107	R147	R340	R120	K452	E111	E113	E203
z_1	-5.49	7.86	7.85	-18.94	-13.50	-13.79	-11.08	-7.93
z_2		8.80	9.17	-16.94		-15.18	-10.00	-9.03
Distances of key residues from S_{int} and S_{cen} in Å								
Residues					K452	E111	R451	
S_{int}					6.27	6.70, 8.21	9.34, 10.29	
S_{cen}					11.6	12.1, 13.0		

Table 1: Above: z locations of charged sites of important residues for 1OTS. Below: distances of key residues from the S_{int} and S_{cen} binding sites.

Potential and shift at S_{int} for different mutations									
111/452	E-K+	E0K+	E-K0	E0K0	K+E-	K+E0	E0E-	K+K+	E-E-
Potential(V)	0.435	0.582	0.190	0.336	0.382	0.513	0.211	1.064	0.085
Shift(V)	0.000	0.147	-0.245	-0.099	-0.053	0.078	-0.224	0.629	-0.350
Potential at S_{int} for 1OTS									
States	default	default+Cl	E113p	E113p+Cl					
Potential(V)	0.230	0.114	0.294	0.178					
Potential at S_{int} for 1OTU									
States	default	default+Cl	E113p	E113p+Cl					
Potential(V)	0.235	0.125	0.296	0.186					

Table 2: Top: potential and shift at S_{int} for different mutations of the 111/452 pair in 1OTU. Middle: potential at S_{int} for 1OTS. Bottom: potential at S_{int} for 1OTU.

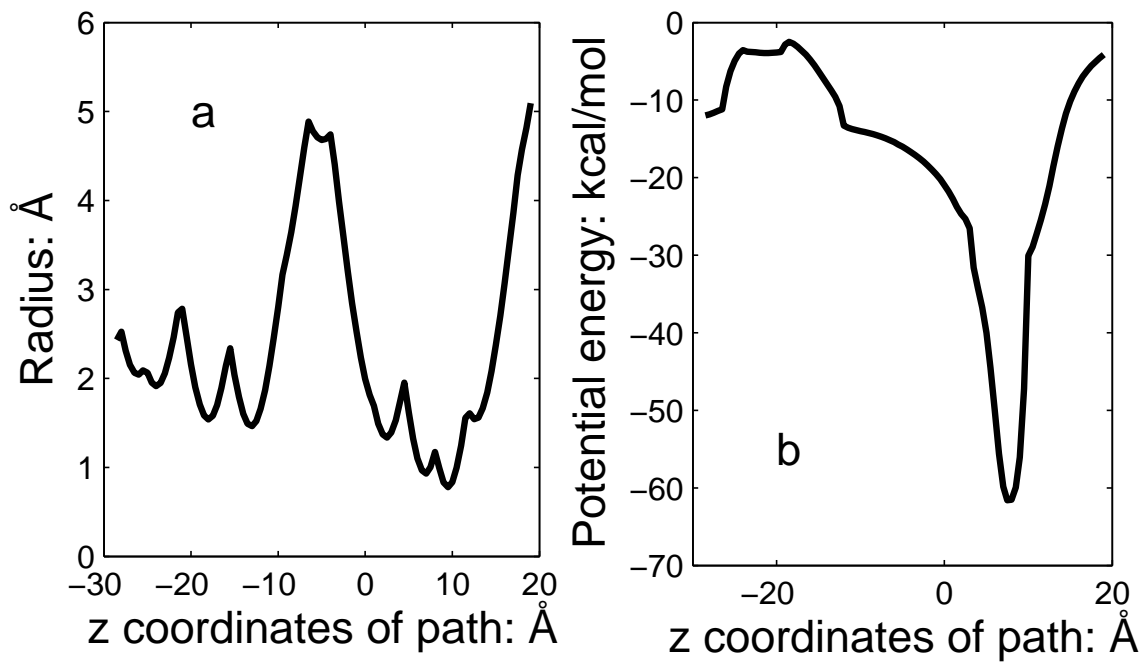


Figure 1: (a) The radius profile for the KcsA potassium channel. (b) The potential profile.

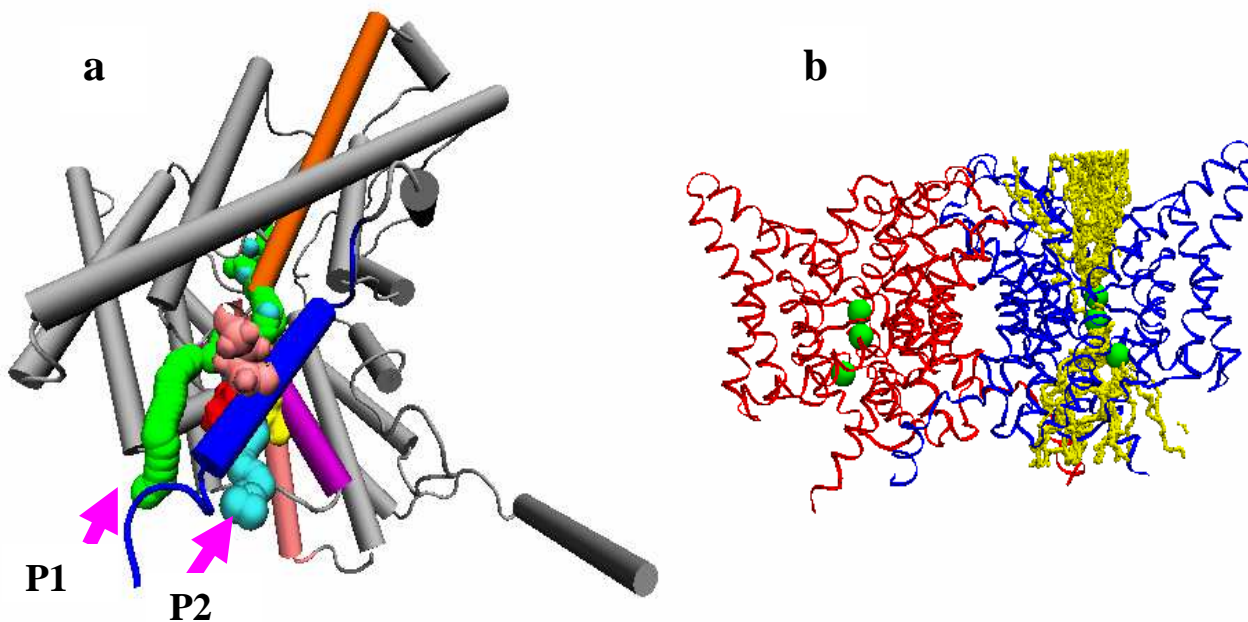


Figure 2: (a) The two wild-type 1OTS anion transit pathways P1 and P2, which differ in the intracellular region. The view is from the side (similar to Fig. 2b), with the protein slightly rotated to display the intracellular vestibule. The P1 path (green) is the vestibular path, while the P2 path (cyan) passes near the D and R helices. Helix R is blue, helix D is purple, helix F is peach, and helix N is rust/orange. Residue E111 is yellow, T452 is red, and R451 is peach, all from the wild-type 1OTS structure. (b) Display of an ensemble of CBMC trajectories (yellow) for the mutant 1OTU structure. Notice the spreading in the two vestibular regions and the constriction through the selectivity filter. The green spheres are the locations of the three anion binding sites.

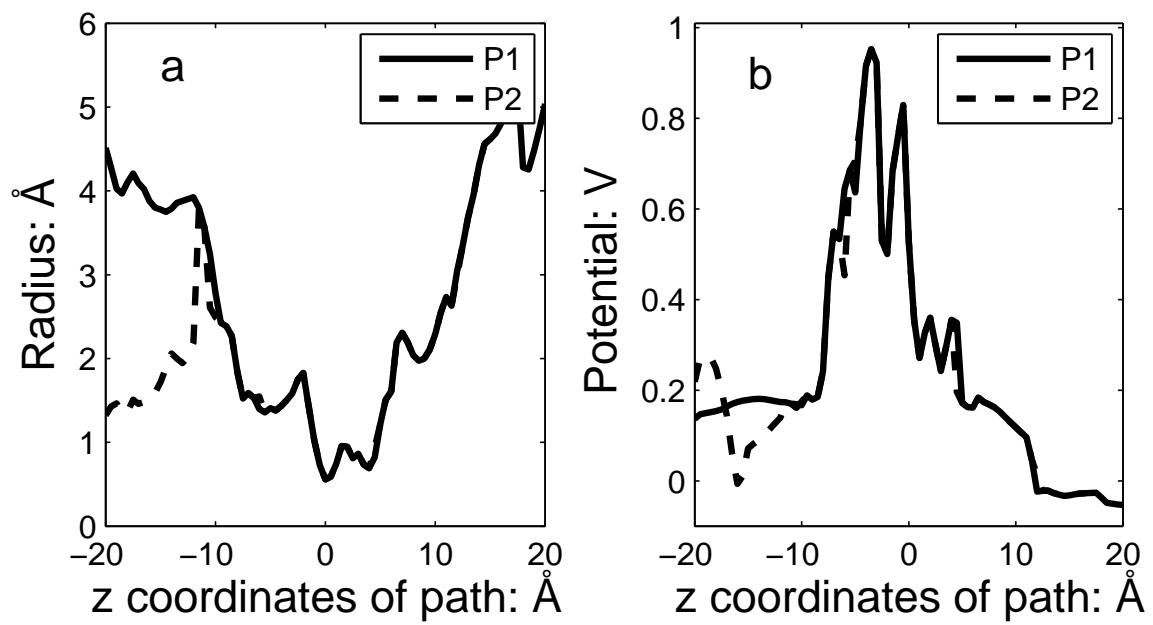


Figure 3: (a) The radius profiles for the two paths P1 and P2 in 1OTS. (b) The potential profiles.